



Ti³⁺ self-doped mesoporous black TiO₂/SiO₂/g-C₃N₄ sheets heterojunctions as remarkable visible-lightdriven photocatalysts

Mengqiao Hu^a, Zipeng Xing^{a,*}, Yan Cao^a, Zhenzi Li^b, Xu Yan^a, Ziyuan Xiu^a, Tianyu Zhao^a, Shilin Yang^{a,*}, Wei Zhou^{a,*}

^a Department of Environmental Science, School of Chemistry and Materials Science, Key Laboratory of Functional Inorganic Material Chemistry, Ministry of Education of PR China, Heilongjiang University, Harbin, 150080, PR China

^b Department of Epidemiology and Biostatistics, Harbin Medical University, Harbin, 150086, PR China, PR China



ARTICLE INFO

Keywords:

Mesoporous TiO₂
Ti³⁺ self-doping
G-C₃N₄ sheet
Heterojunction
Visible-light-driven photocatalysis

ABSTRACT

Ti³⁺ self-doped mesoporous black TiO₂/SiO₂/g-C₃N₄ sheets heterojunctions are successfully prepared by a sol-gel strategy, followed by calcination at 450 °C and hydrogenation at 500 °C. The characterization results indicate that Ti³⁺ self-doped mesoporous black TiO₂/SiO₂/g-C₃N₄ sheets heterojunctions photocatalysts possess high surface area of ~145.6 m² g⁻¹, large pore size of ~4 nm and pore volume of ~0.27 cm³ g⁻¹, respectively. The complete retention of the mesoporous frameworks is attributed to the addition of SiO₂, which not only retards the growth of TiO₂ crystals but also avoids the collapse of the channels even under high temperature calcination process. The prepared heterojunctions photocatalysts with narrow bandgap of ~2.25 eV exhibit the excellent photocatalytic activity for degradation of phenol (98.5%), reduction of Cr⁶⁺ (97%) and photocatalytic hydrogen evolution (572.6 μmol h⁻¹ g⁻¹) under visible light irradiation, which is several times higher than that of pristine one. The outstanding photocatalytic property can be ascribed to the unique mesoporous framework enhancing the adsorption of pollutants and favoring the mass transfer, Ti³⁺ self-doping reducing the bandgap and extending the photoresponse to visible light region, the formation of heterojunctions preventing the recombination of photogenerated electrons and holes and benefiting their effective separation.

1. Introduction

With the emergence of energy crisis and environmental pollution, mesoporous TiO₂ materials have gradually aroused a great deal of attention due to their promising applications in photocatalysis for degradation of pollutants and H₂ evolution from water splitting, dye-sensitized solar cells, sensors and other fields [1–3]. As a typical photocatalytic material, researchers are dedicated to designing and developing mesoporous TiO₂ due to its fascinating properties, such as large specific surface area, transparent open porous channels, adequate surface active sites [4–6]. However, the stability of mesoporous TiO₂ has a very thorny issue, which is urgently needed to be solved [7]. In the majority of cases, the pore channels of mesoporous TiO₂ are prone to collapse at calcination temperature up to 400 °C owing to the intrinsic crystallization of mesoporous TiO₂ crystals [8]. Therefore, in order to figure out the problem of weak stability of mesoporous TiO₂ materials, it is proposed that SiO₂ is added to the mesoporous TiO₂ framework to protect the integrity of the mesoporous structure even at high temperature treatment process because the addition of SiO₂ can effectively

delay the growth of TiO₂ crystals [9,10].

The introduction of SiO₂ not only retard the growth of mesoporous TiO₂ crystals, but also further improve the specific surface area of the catalyst in order to facilitate the subsequent photocatalytic reaction [11]. However, only UV light (~4% of the sunlight) can stimulate the photoresponse of mesoporous TiO₂ due to its large energy threshold value for visible light response (band gap of ~3.2 eV), which severely limits the practical applications of mesoporous TiO₂ [12,13]. Meanwhile, the fast recombination rate of photogenerated charge and hole also greatly reduces the photocatalytic activity [14]. Therefore, many methods have been devoted to modifying mesoporous TiO₂ materials to effectively improve the visible response and further promote the photocatalytic reaction, including elements doping [15], semiconductor coupling [16], surface sensitization [17], and so on. Among them, the semiconductor coupling has been proven as an effective strategy to enhance the separation of electrons and holes [18].

Recently, graphite-like carbon nitride (g-C₃N₄) with folded sheet structure has become a hot topic in the past decade duo to the fact that it is an organic semiconductor with the response to visible light and

* Corresponding authors.

E-mail addresses: xingzipeng@hlju.edu.cn (Z. Xing), yangshilin@hlju.edu.cn (S. Yang), zhouwei1@hlju.edu.cn (W. Zhou).

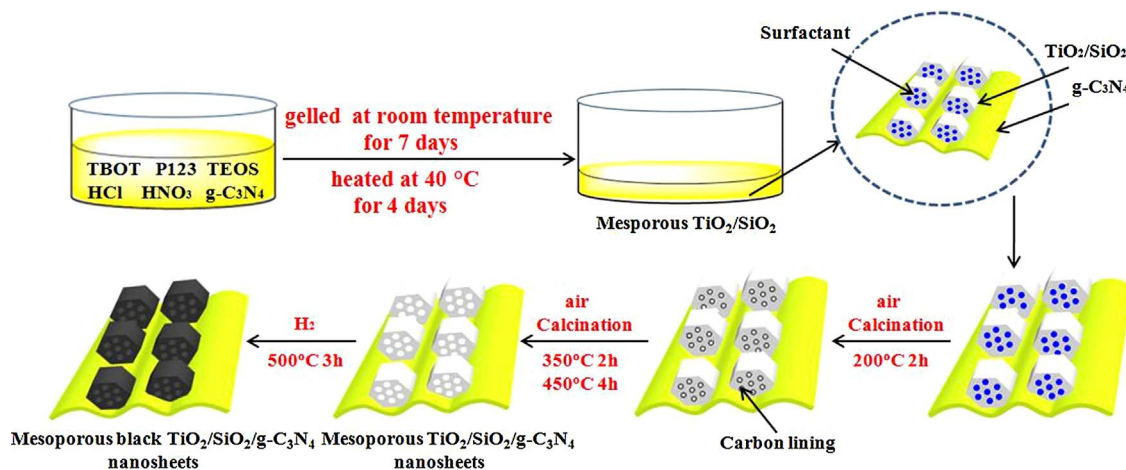


Fig. 1. Schematic diagram for the formation of bm-TiO₂/SiO₂/g-C₃N₄ sheets heterojunctions architecture.

strong reduction activity. The band-gap of g-C₃N₄ is ~2.7 eV and it has been proposed as a potential candidate to produce hydrogen and degrade contaminants under visible light irradiation [19]. However, the problem with the high recombination rate of photogenerated electrons and holes restricts the applications of g-C₃N₄ [20]. Coupling g-C₃N₄ with other materials to improve photocatalytic activity is a perfect strategy because photogenerated charge can quickly transfer through across the interface of the heterostructure to hinder the recombination of photogenerated electrons and holes [21]. Among various materials, mesoporous TiO₂ is the most preferred material for coupling with g-C₃N₄ to reinforce the separation of electrons and holes and increase photocatalytic performance [22].

To further extend the absorption of light into the visible region of mesoporous TiO₂, the intrinsic band gap of mesoporous TiO₂ must be greatly shortened. In recent years, more and more work had been committed to changing the color of TiO₂ to improve the absorption of visible light [23,24]. In 2011, Mao et al. presented a pioneering research that the super high-active performance black TiO₂ was successfully synthesized by the method of hydrogenation. The resultant hydrogenated black TiO₂ with a narrow bandgap showed a pretty amazing photocatalytic capacity compared to white TiO₂, which can attributed to the introducing of Ti³⁺ and the forming of oxygen vacancies in the process of high temperature hydrogenation [25]. The synergistic effect can effectively reduce the width of the bandgap and improve the visible light response because the formation of the new electron energy levels is below the conduction band of TiO₂ [26]. Since then, more and more efforts have been devoted to designing and developing of black TiO₂ in order to pursue high-performance photocatalytic materials [27,28]. Although the research of individual mesoporous TiO₂, black TiO₂, and g-C₃N₄ has been quite mature, it is rare to combine them through a simple and reliable way, in other words, this is still an immeasurable challenge.

Herein, we report a facile a sol-gel strategy, followed by calcination at 450 °C and hydrogenation at 500 °C, for synthesizing Ti³⁺ self-doped mesoporous black TiO₂/SiO₂/g-C₃N₄ sheets heterojunctions. The morphology, structure, and properties of the samples are also analyzed and tested in detail. The synthesized samples exhibit excellent photocatalytic properties for the degradation of phenol, Cr⁶⁺, and hydrogen production. Finally, the photocatalytic mechanism is also proposed.

2. Experimental

2.1. Materials

Tetrabutyltitanate (TBOT), tetraethyl orthosilicate (TEOS), absolute ethanol (EtOH), concentrated nitric acid (HNO₃) and concentrated

hydrochloric acid (HCl) were purchased from Tian-jin Kermel Chemical Reagent Co. Ltd, China. Pluronic P123 was purchased from Sigma-Aldrich. All the reagents used were analytical grade and employed without further purification.

2.2. Synthesis

2.2.1. Synthesis of g-C₃N₄ sheets

The melamine was placed into an alumina crucible and calcined at 550 °C for 4 h in a muffle furnace under air atmosphere. After cooling down to room temperature, the yellow g-C₃N₄ sheets were formed.

2.2.2. Synthesis of mesoporous TiO₂/SiO₂/g-C₃N₄ sheets heterojunctions

The Ti³⁺ self-doped mesoporous black TiO₂/SiO₂/g-C₃N₄ sheet composite materials were synthesized by a sol-gel method, followed by calcination at 450 °C and hydrogenation at 500 °C. According to previous report [29], we prepared a mixed solution of the mesoporous TiO₂/SiO₂ sample, and then 0.85 g of g-C₃N₄ powder was added to the aforementioned mixture and stirred for at least 120 min. Thereafter, the resulting solution was gelled at room temperature in an open petri dish for a week and then transferred to an oven at 40 °C for four days. The resulting samples were washed and then dried at 60 °C overnight, followed by calcining. The calcination process involves calcination at different temperatures and the specific process was based on our published literature [9]. Finally, the faint yellow powders were prepared and named as m-TiO₂/SiO₂/g-C₃N₄. For comparison, the pure mesoporous TiO₂/SiO₂ was obtained in the absence of g-C₃N₄ and named as m-TiO₂/SiO₂.

2.2.3. Synthesis of Ti³⁺ self-doped mesoporous black TiO₂/SiO₂/g-C₃N₄ sheets heterojunctions

The faint yellow m-TiO₂/SiO₂/g-C₃N₄ powder was calcined at 500 °C for 3 h and was always accompanied by hydrogen penetration. Finally, the Ti³⁺ self-doped mesoporous black m-TiO₂/SiO₂/g-C₃N₄ sheets heterojunctions materials were successfully synthesized and named as bm-TiO₂/SiO₂/g-C₃N₄ (Fig. 1).

2.3. Characterization

The X-ray diffraction (XRD-D8 Advance, Bruker) technique with Cu K α radiation ($\lambda = 1.5406 \text{ \AA}$), coupled with emission current of 30 mA. Using KBr as diluents, the Fourier transform infrared spectra (FT-IR) of the samples were collected with a PerkinElmer spectrum one system. Scanning electron microscopy (SEM) images were obtained with a Philips XL-30-ESEM-FEG instrument. Transmission electron microscopy (TEM) was performed using a JEM-2100 electron microscope (JEOL,

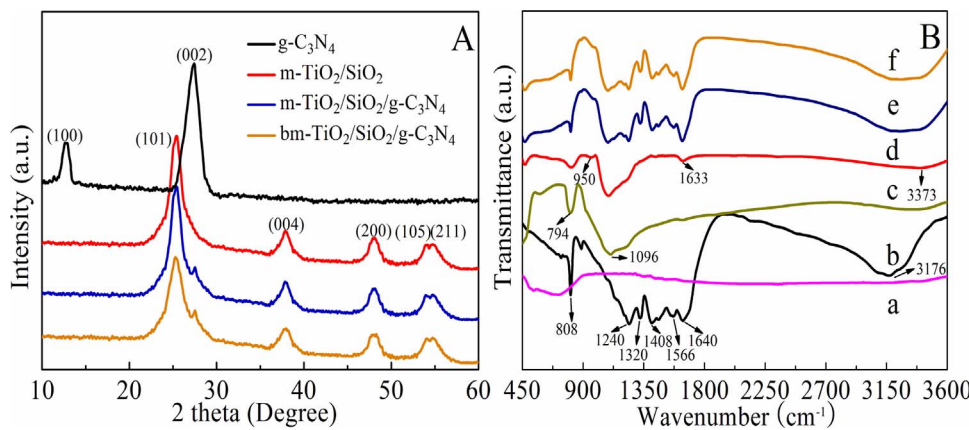


Fig. 2. XRD patterns (A) and FT-IR spectra (B) of TiO₂ (a), g-C₃N₄ (b), SiO₂ (c), m-TiO₂/SiO₂ (d), m-TiO₂/SiO₂/g-C₃N₄ (e), and m-TiO₂/SiO₂/g-C₃N₄ (f), respectively.

Japan). Brunauer-Emmett-Teller (BET) with an AUTOSORB-1 (Quantachrome Instruments) nitrogen adsorption apparatus was used to test surface area determination. The PHI-5700 ESCA instrument with Al-K_α X-ray source was hired to analyze the data of X-ray photoelectron spectroscopy (XPS). The UV-vis diffuse reflectance spectra (DRS) were obtained from a TU-1901 spectrophotometer and BaSO₄ was chosen as the reference. The electron paramagnetic resonance (EPR) spectra is obtained by a JES-FA200 X band spectrometer. The total organic carbon (TOC) removal was tested by the TOC analysis equiped with analytic jena multi NIC 2100 analyzer. The Electron spin resonance (ESR) spectra were recorded by a Bruker model A300 spectrometer under visible light irradiation. The settings of the ESR spectrometer were as followed: center field = 3512 G, microwave frequency = 9.42 GHz, microwave power = 20 mW. The ·OH radicals was tested by the terephthalic acid photoluminescence on a RF-5301PC fluorescence spectrophotometer. The electrochemical impedance spectroscopy (EIS) was carried out with IM6e Impedance measurement unit. Scanning Kelvin probe (SKP) test (SKP5050 system, Scotland) was executed to evaluate the work function at ambient atmosphere.

2.4. Photocatalytic test

2.4.1. Photocatalytic degradation

The photocatalytic performance was studied by the degradation of phenol and reduction of Cr⁶⁺ under visible light irradiation by using a 300 W Xeon-lamp equipped with a 420 nm cut-off filter. Simply, 35 mg of photocatalysts mixed with 25 mL of 10 mg L⁻¹ phenol solution and the mixed solution was put at 20 cm from the light source. Before the visible light, the mixed solution was stirred in the dark for 30 min to ensure the adsorption-desorption equilibrium. At the same time intervals, the part of the mixture was centrifuged and separated. Consequently, using a T6 UV-vis spectrophotometer, the concentration of phenol was analyzed. The photocatalytic reduction process of Cr⁶⁺ was the same as the process of degradation of phenol. However, the concentration of Cr⁶⁺ was measured by 1,5-Diphenylcarbohydrazide spectrophotometric method using UV-vis spectrophotometer.

2.4.2. Photocatalytic hydrogen evolution

Photocatalytic hydrogen production test was executed in an online photocatalytic hydrogen generation system at room temperature (AuLight, Beijing, CEL-SPH2N). The methanol and Pt were used as sacrificial agent and cocatalyst. The 50 mg of photocatalysts were placed in a 100 mL of aqueous solution containing 80 mL of deionized water and 20 mL of methanol in closed-gas circulation reaction cell. Before the reaction, in order to completely dislodge O₂ and CO₂, the system was vacuumized using passing N₂. Consequently, the mixture solution was irradiated by a 300 W Xeon-lamp equipped with an AM 1.5 G filter (Oriel, USA). Finally, using an on-line gas chromatography with the interval of each 1 h (SP7800, TCD, molecular sieve 5 Å, N₂ carrier,

Beijing Keruida, Ltd) periodically measure the production of hydrogen.

2.5. Photoelectrochemical measurement

Using an electrochemical workstation that had a standard three-electrode system tested the photoelectrochemical measurements (CHI760E, Shanghai). The 50 mg of photocatalyst sample was added in to 35 mL of terpineol with the vigorously stirring to prepare the experimental electrode. The mixture was dip-coated onto the FTO electrode and then calcined at 200 °C for 120 min. The working electrode, counter electrode and reference electrode were the as-prepared photocatalyst, Pt sheet and Ag/AgCl, respectively. The electrolyte was 1 M KOH solution and the light source was a 300 W Xenon-lamp with a 420 nm cut off filter.

3. Results and discussion

TiO₂ has three different crystal phases, and different crystals have different effects on photocatalysis, which can further affect its practical application [30]. Therefore, XRD is employed to determine the phase structures of these as-prepared samples. In Fig. 2A, the XRD characteristic peaks of g-C₃N₄ are observed at around 13.0 and 27.4°, which can be ascribed to the (100) and (002) plane of g-C₃N₄. The phase composition of m-TiO₂/SiO₂ is characterized by five diffraction peaks at around 25.3, 37.8, 48.1, 54.1, and 54.9° are attributed to the (101), (004), (200), (105), and (211), respectively. Otherwise, all the characteristic peaks of m-TiO₂/SiO₂/g-C₃N₄ and bm-TiO₂/SiO₂/g-C₃N₄ samples correspond to the original diffraction peaks of m-TiO₂/SiO₂ and g-C₃N₄, indicating that m-TiO₂/SiO₂ and g-C₃N₄ have been successfully compound and the original structure of m-TiO₂/SiO₂ sample is fairly stable and can not be easily changed even after high temperature hydrogenation. However, the bm-TiO₂/SiO₂/g-C₃N₄ diffraction peaks reveals a slightly attenuation and extension compared to m-TiO₂/SiO₂/g-C₃N₄ sample, which can be ascribed to the production of Ti³⁺ and oxygen vacancy after hydrogenation [31]. Obviously, the diffraction peaks of SiO₂ are not seen because SiO₂ belongs to amorphous structure.

The chemical structure of the complex photocatalyst is executed by FT-IR in order to compare with the individual chemical constituent, as illustrated in Fig. 2B. For mesoporous TiO₂, the primary vibration peaks at 450–700 cm⁻¹ is assigned to the oscillation of Ti–O–Ti of mesoporous TiO₂, while the peaks at 1633 and 3373 cm⁻¹ are attributed to the surface-bonded –OH groups or surface- adsorbed H₂O molecular. For the pure SiO₂, the characteristic peaks at 794 and 1096 cm⁻¹ can be corresponded to Si–O–Si symmetric stretching and Si–O–Si asymmetric stretching vibrations, respectively [32]. As for g-C₃N₄, the band at 808 and 3176 cm⁻¹ are observed, which are associated with the breathing mode of triazine units and the stretching vibration mode of N–H, while a series of absorption peaks located at 1200–1650 cm⁻¹

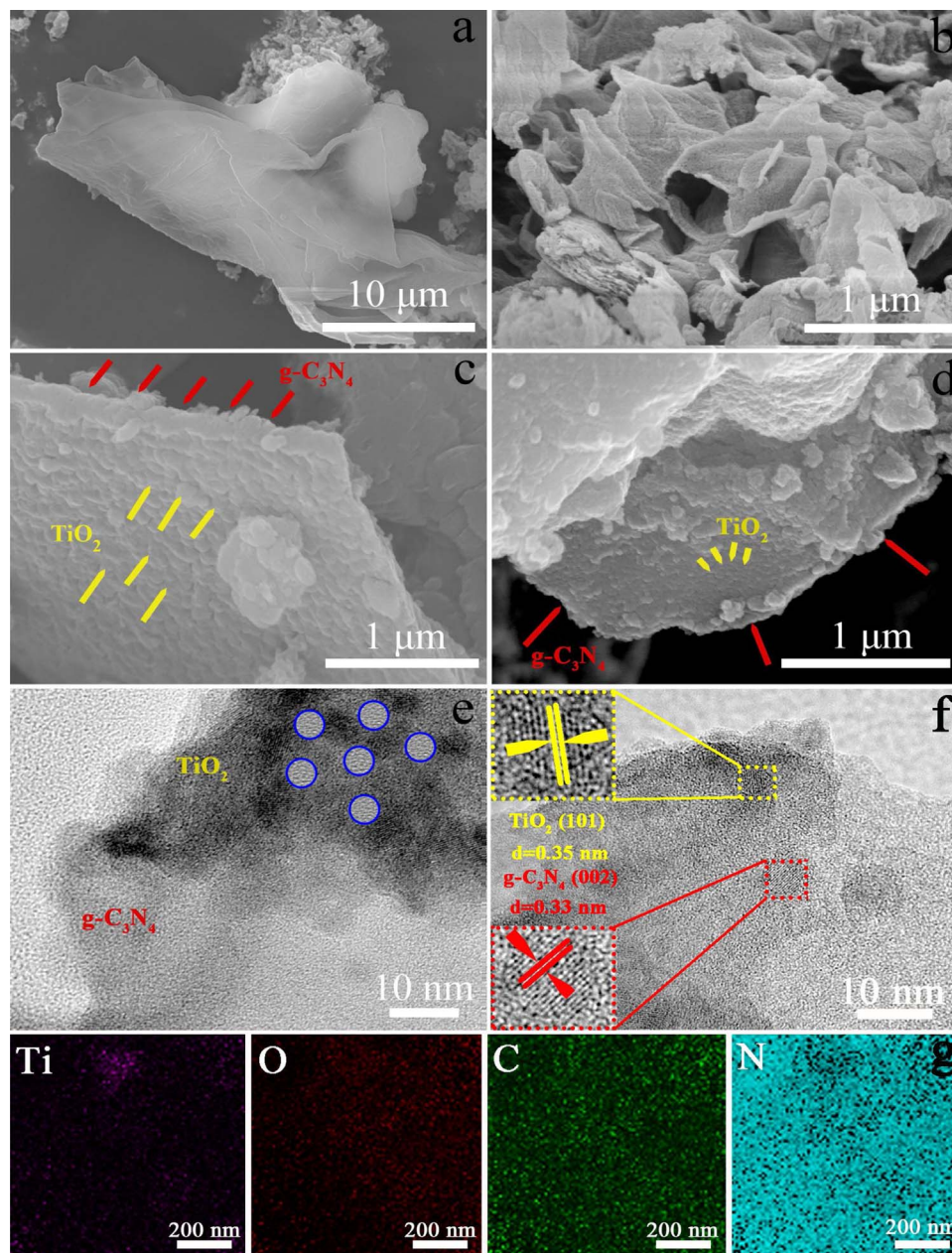


Fig. 3. SEM images of $g\text{-C}_3\text{N}_4$ (a, b) and $bm\text{-TiO}_2/\text{SiO}_2/g\text{-C}_3\text{N}_4$ (c, d), TEM images of $bm\text{-TiO}_2/\text{SiO}_2/g\text{-C}_3\text{N}_4$ (e, f), and the corresponding elemental mapping of Ti, O, C, and N, respectively (g).

can originate from the typical stretching modes of the C–N heterocycles [33]. In the FT-IR spectrum of $m\text{-TiO}_2/\text{SiO}_2$, it can be clearly observed that the characteristic peaks of $m\text{-TiO}_2/\text{SiO}_2$ sample are derived from the characteristic peaks of mesoporous TiO_2 and SiO_2 samples. However, the only difference is that a special characteristic peak appears dramatically at 950 cm^{-1} , which correspond to the bond of Si-O-Ti [34], it can further mean that the SiO_2 has been successfully incorporated into the frame of TiO_2 . In the FT-IR spectrum of $m\text{-TiO}_2/\text{SiO}_2/g\text{-C}_3\text{N}_4$ and $bm\text{-TiO}_2/\text{SiO}_2/g\text{-C}_3\text{N}_4$, all characteristic peaks of $m\text{-TiO}_2/\text{SiO}_2$ and $g\text{-C}_3\text{N}_4$ exist in $m\text{-TiO}_2/\text{SiO}_2/g\text{-C}_3\text{N}_4$ and $bm\text{-TiO}_2/\text{SiO}_2/g\text{-C}_3\text{N}_4$, implying that $m\text{-TiO}_2/\text{SiO}_2/g\text{-C}_3\text{N}_4$ have perfectly combined, and the composition of the $bm\text{-TiO}_2/\text{SiO}_2/g\text{-C}_3\text{N}_4$ is not affected during the high temperature hydrogenation process.

The morphology and microstructure are characterized by SEM and TEM. From Fig. 3a and b, it can be unambiguously observed that $g\text{-C}_3\text{N}_4$ exhibits a two-dimensional (2D) lamellar structure with plicated surface, which is in size of several micrometers. The SEM image of $bm\text{-TiO}_2/\text{SiO}_2/g\text{-C}_3\text{N}_4$ is presented in Fig. 3c and d. Obviously, when black mesoporous $\text{TiO}_2/\text{SiO}_2$ is added, the surface of $g\text{-C}_3\text{N}_4$ becomes rougher

compared with the individual $g\text{-C}_3\text{N}_4$, which can indicate that black mesoporous $\text{TiO}_2/\text{SiO}_2$ has uniformly loaded on the surface of $g\text{-C}_3\text{N}_4$ to form a new complex heterostructures between $bm\text{-TiO}_2/\text{SiO}_2$ and $g\text{-C}_3\text{N}_4$. What's more, the TEM images of $bm\text{-TiO}_2/\text{SiO}_2/g\text{-C}_3\text{N}_4$ after hydrogenation at $500\text{ }^\circ\text{C}$ are depicted in Fig. 3e and f. The plicated $g\text{-C}_3\text{N}_4$ sheets are loaded by black mesoporous $\text{TiO}_2/\text{SiO}_2$ with a diameter of $\sim 4\text{ nm}$ (blue circle area). In order to clearly observe the lattice spacing, the lattice fringe areas of TiO_2 (the yellow area) and $g\text{-C}_3\text{N}_4$ (the red area) are enlarged. The lattice spacing of 0.35 and 0.33 nm can be found, which matches to the (101) plane of anatase phase and (002) plane of $g\text{-C}_3\text{N}_4$, respectively. Notably, some cross lattice fringes that are marked by the red and yellow line are distinctly observed, revealing that the heterojunctions between $bm\text{-TiO}_2/\text{SiO}_2$ and $g\text{-C}_3\text{N}_4$ are successfully formed. The formation of this heterostructure can be considered as a forceful testimony to accelerate photoinduced charge transfer and improve photocatalytic efficiency. To prove the mesoporous $\text{TiO}_2/\text{SiO}_2$ uniformly loaded on the surface of $g\text{-C}_3\text{N}_4$ sheet, the SEM mapping of corresponding elements in the $\text{TiO}_2/\text{SiO}_2/g\text{-C}_3\text{N}_4$ composite is shown in Fig. 3g. It can be clearly seen that the Ti, O, C,

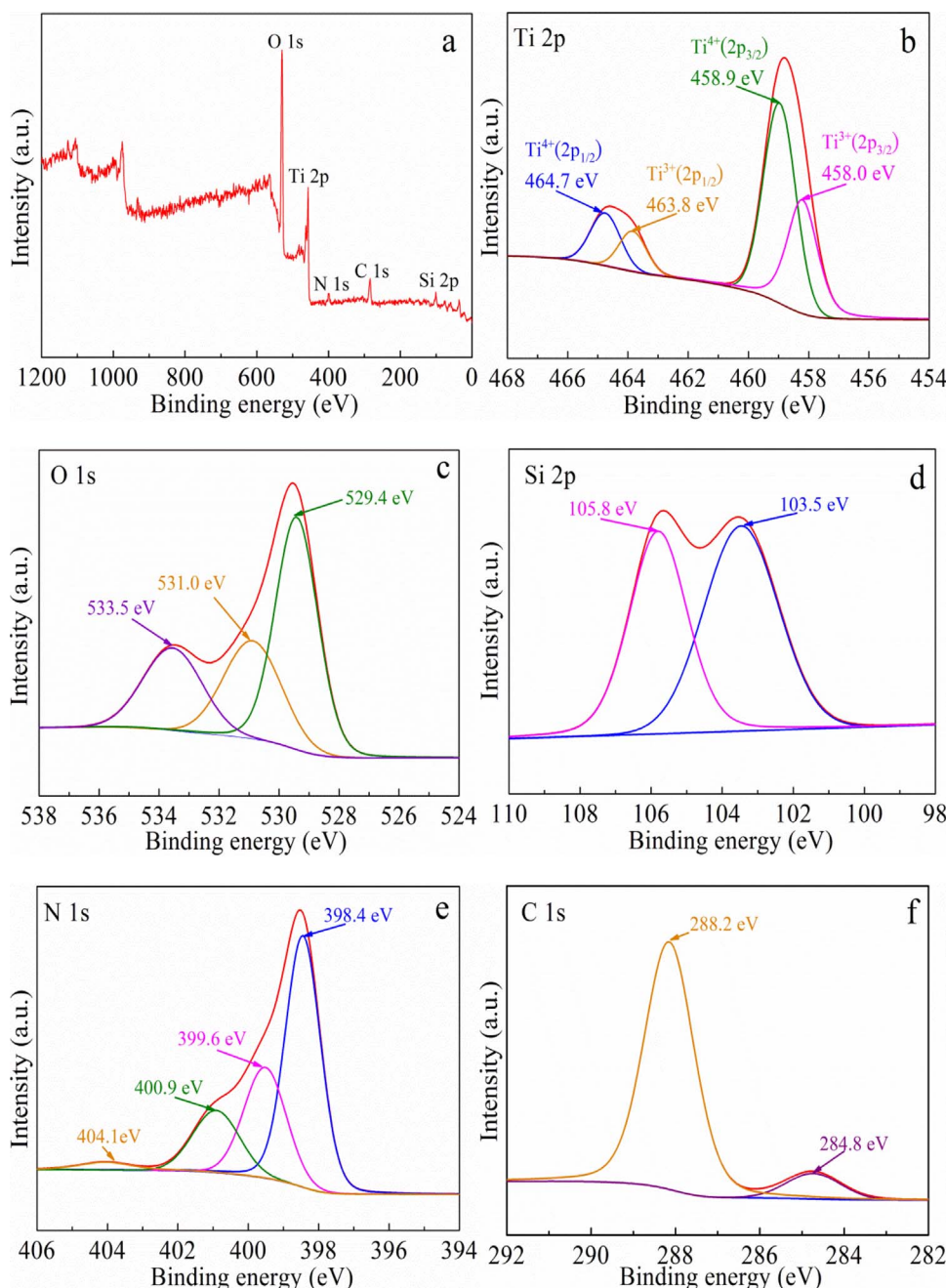


Fig. 4. The full-scale XPS spectra (a), Ti 2p (b), O 1s (c), Si 2p (d), N 1s (e), C 1s (f) of bm-TiO₂/SiO₂/g-C₃N₄, respectively.

and N elements are highly uniform in the system, demonstrating that the mesoporous TiO₂/SiO₂ has been uniformly loaded on the outer layer of g-C₃N₄ sheet. More importantly, the uniform exposure of black mesoporous TiO₂/SiO₂ particles on the surface of g-C₃N₄ can facilitate the capture and utilization of visible light efficiently.

XPS is employed to investigate the elemental compositions and chemical states of the resultant crystal of bm-TiO₂/SiO₂/g-C₃N₄, and the results are described in Fig. 4. From Fig. 4a, the XPS survey spectrum of the bm-TiO₂/SiO₂/g-C₃N₄ composite material can verify the existence of Ti, O, Si, C, and N elements. Fig. 4b shows the Ti 2p XPS spectra of the bm-TiO₂/SiO₂/g-C₃N₄, the peak binding energies at 464.7, 463.8, 458.9, and 458.0 eV can be attributed to Ti⁴⁺ 2p_{1/2}, Ti³⁺ 2p_{1/2}, Ti⁴⁺ 2p_{3/2}, and Ti³⁺ 2p_{3/2}, respectively, implying that Ti³⁺ are created as a result of the Ti⁴⁺ reduction of TiO₂ through the hydrogenation [35]. Three peaks are observed at 533.5, 531.0, and 529.4 eV in the XPS spectrum of O 1s (Fig. 4c), which can be assigned to –OH groups, Si-O-Si, and Ti–O–Ti bonds, respectively [29,36]. As can be

seen from Fig. 4d, the peaks of Si 2p at 105.8 and 103.5 eV are derived from Ti-O-Si and the formation of Si-O-Si bond, respectively [37]. Fig. 4e can describe the XPS of bm-TiO₂/SiO₂/g-C₃N₄ in the N 1s binding energy regions, and the regions are divided into four peaks, in which the peaks at the binding energy of 400.9, 399.6, and 398.4 eV are related to C–N–H groups, tertiary nitrogen N–(C)₃ groups, and the sp²-hybridized N (C=N–C), respectively. The peak located at 404.1 eV can originate from charging effects [38]. The C 1s XPS spectra of the bm-TiO₂/SiO₂/g-C₃N₄ is exhibited in Fig. 4f, the peak can be separated into two peaks at 284.8 and 288.2 eV, corresponding to adventitious carbon C–C and N–C=N, respectively, which are the dominant carbon species in the g-C₃N₄ [39]. According to the analysis and discussion, it can be concluded that Ti³⁺ species have been successfully introduced and the heterojunctions are also successfully compounded.

The N₂ adsorption-desorption isotherms and the pore size distribution curves of g-C₃N₄, m-TiO₂/SiO₂, m-TiO₂/SiO₂/g-C₃N₄, and bm-TiO₂/SiO₂/g-C₃N₄ composite photocatalysts are measured in Fig. 5a

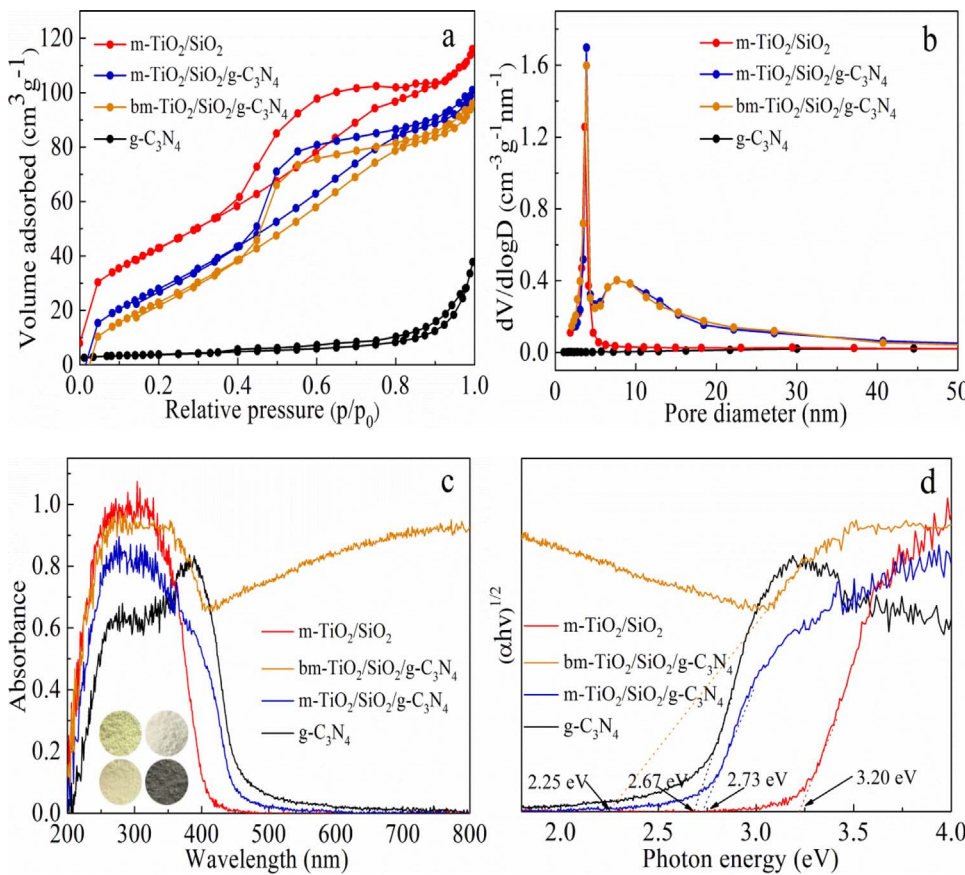


Fig. 5. N_2 adsorption-desorption isotherm curves (a), BJH pore size distribution plots (b) UV-vis diffuse reflectance spectra (c), and the corresponding bandgaps (d) of $g\text{-}C_3\text{N}_4$, $m\text{-}TiO_2\text{/SiO}_2$, $m\text{-}TiO_2\text{/SiO}_2\text{/g-}C_3\text{N}_4$, and $bm\text{-}TiO_2\text{/SiO}_2\text{/g-}C_3\text{N}_4$, respectively. The insets of (c) are photos of these samples.

and b, respectively. From Fig. 5a, the specific surface area of $g\text{-}C_3\text{N}_4$ is only $13.5\text{ m}^2\text{ g}^{-1}$, and no typical type IV curve is observed [40], indicating that the $g\text{-}C_3\text{N}_4$ sample is nonporous. Exhilaratingly, it is obvious that the $m\text{-}TiO_2\text{/SiO}_2$, $m\text{-}TiO_2\text{/SiO}_2\text{/g-}C_3\text{N}_4$, and $bm\text{-}TiO_2\text{/SiO}_2\text{/g-}C_3\text{N}_4$ show typical type IV isotherms with an obvious hysteresis loop, which is a strong reason to prove that the $m\text{-}TiO_2\text{/SiO}_2$, $m\text{-}TiO_2\text{/SiO}_2\text{/g-}C_3\text{N}_4$, and $bm\text{-}TiO_2\text{/SiO}_2\text{/g-}C_3\text{N}_4$ photocatalysts are mesoporous structure. The surface area and pore volume of the $m\text{-}TiO_2\text{/SiO}_2$ material synthesized by the sol-gel way are as high as $161.2\text{ m}^2\text{ g}^{-1}$ and $0.30\text{ cm}^3\text{ g}^{-1}$, respectively. Besides, the specific surface area and pore volume of $m\text{-}TiO_2\text{/SiO}_2\text{/g-}C_3\text{N}_4$ are $148.1\text{ m}^2\text{ g}^{-1}$ and $0.27\text{ cm}^3\text{ g}^{-1}$ and slightly decreased compared with the original $m\text{-}TiO_2\text{/SiO}_2$ sample. This decrease is due to the fact that the efficient combination of the $g\text{-}C_3\text{N}_4$. Simultaneously, we can see that the specific surface area and pore volume of the $bm\text{-}TiO_2\text{/SiO}_2\text{/g-}C_3\text{N}_4$ sample are $145.6\text{ m}^2\text{ g}^{-1}$ and $0.27\text{ cm}^3\text{ g}^{-1}$ after hydrogenation, respectively, which is almost the same as the original white one. From Fig. 5b, the pore size of $m\text{-}TiO_2\text{/SiO}_2$ is $\sim 4\text{ nm}$ and demonstrates a narrow pore size distribution, indicating that mesoporous structure with uniform and regular pores is present. The $m\text{-}TiO_2\text{/SiO}_2\text{/g-}C_3\text{N}_4$ and $bm\text{-}TiO_2\text{/SiO}_2\text{/g-}C_3\text{N}_4$ samples retain the original uniform pore channel (Table 1), indicating that the

mesoporous structure of $m\text{-}TiO_2\text{/SiO}_2\text{/g-}C_3\text{N}_4$ is fairly stable owing to the adding of SiO_2 , which can effectively delay the growth of TiO_2 and prevent the collapse of the hole channel. However, a peak appears at 7.8 nm due to the mutual accumulation between $bm\text{-}TiO_2\text{/SiO}_2$ and $g\text{-}C_3\text{N}_4$.

To assess the visible light absorption abilities and bandgap of $g\text{-}C_3\text{N}_4$, $m\text{-}TiO_2\text{/SiO}_2$, $m\text{-}TiO_2\text{/SiO}_2\text{/g-}C_3\text{N}_4$, and $bm\text{-}TiO_2\text{/SiO}_2\text{/g-}C_3\text{N}_4$ composites, the UV-vis diffuse reflectance spectra (DRS) is investigated, as shown in Fig. 5c. As for the $g\text{-}C_3\text{N}_4$, it exhibits a wide photoabsorption from UV to visible light and the absorption edge is up to nearly 490 nm , as a result of $g\text{-}C_3\text{N}_4$ relatively narrow bandgap. Nevertheless, the $m\text{-}TiO_2\text{/SiO}_2$ shows the basal absorption edge rising at 400 nm (UV region) due to the wide bandgap. After coupling with $g\text{-}C_3\text{N}_4$, the $m\text{-}TiO_2\text{/SiO}_2\text{/g-}C_3\text{N}_4$ sample shows an obvious absorption for visible light and the absorption edge extends to 460 nm . Moreover, compared with $m\text{-}TiO_2\text{/SiO}_2\text{/g-}C_3\text{N}_4$ sample, the $bm\text{-}TiO_2\text{/SiO}_2\text{/g-}C_3\text{N}_4$ sample shows a further enhancement for the absorption of visible light, which can be attributed to the synergistic effect between mesoporous construction of TiO_2 , $g\text{-}C_3\text{N}_4$ with sheets structure, and the doping of Ti^{3+} [41]. It has been reported that Ti^{3+} and oxygen vacancy can break the selection rule for indirect transitions of TiO_2 , shorten the bandgap and increase absorption of photon energy [42]. From the inset of Fig. 5c, the color of $g\text{-}C_3\text{N}_4$, $m\text{-}TiO_2\text{/SiO}_2$, $m\text{-}TiO_2\text{/SiO}_2\text{/g-}C_3\text{N}_4$, and $bm\text{-}TiO_2\text{/SiO}_2\text{/g-}C_3\text{N}_4$ are yellow, white, faint yellow, and black, respectively. Furthermore, the bandgaps of these samples are calculated in Fig. 5d. The bandgaps of $g\text{-}C_3\text{N}_4$, $m\text{-}TiO_2\text{/SiO}_2$, $m\text{-}TiO_2\text{/SiO}_2\text{/g-}C_3\text{N}_4$, and $bm\text{-}TiO_2\text{/SiO}_2\text{/g-}C_3\text{N}_4$ are 2.67 , 3.20 , 2.73 , and 2.25 eV , respectively. Among them, the $bm\text{-}TiO_2\text{/SiO}_2\text{/g-}C_3\text{N}_4$ semiconductor material with the narrowest bandgap can have a strong absorption for visible light and effectively promote subsequent photocatalytic reactions, as discussed below.

The photocatalytic performance of these samples is tested by testing the degradation of phenol and reduction of Cr^{6+} under visible light

Table 1

BET surface areas, pore sizes, and pore volumes of $m\text{-}TiO_2\text{/SiO}_2$, $m\text{-}TiO_2\text{/SiO}_2\text{/g-}C_3\text{N}_4$, and $bm\text{-}TiO_2\text{/SiO}_2\text{/g-}C_3\text{N}_4$, respectively.

Sample	BET surface area ($\text{m}^2\text{ g}^{-1}$)	Pore size (nm)	Pore volume ($\text{cm}^3\text{ g}^{-1}$)
$m\text{-}TiO_2\text{/SiO}_2$	161.2	4.07	0.30
$m\text{-}TiO_2\text{/SiO}_2\text{/g-}C_3\text{N}_4$	148.1	4.06	0.27
$bm\text{-}TiO_2\text{/SiO}_2\text{/g-}C_3\text{N}_4$	145.6	4.06	0.27

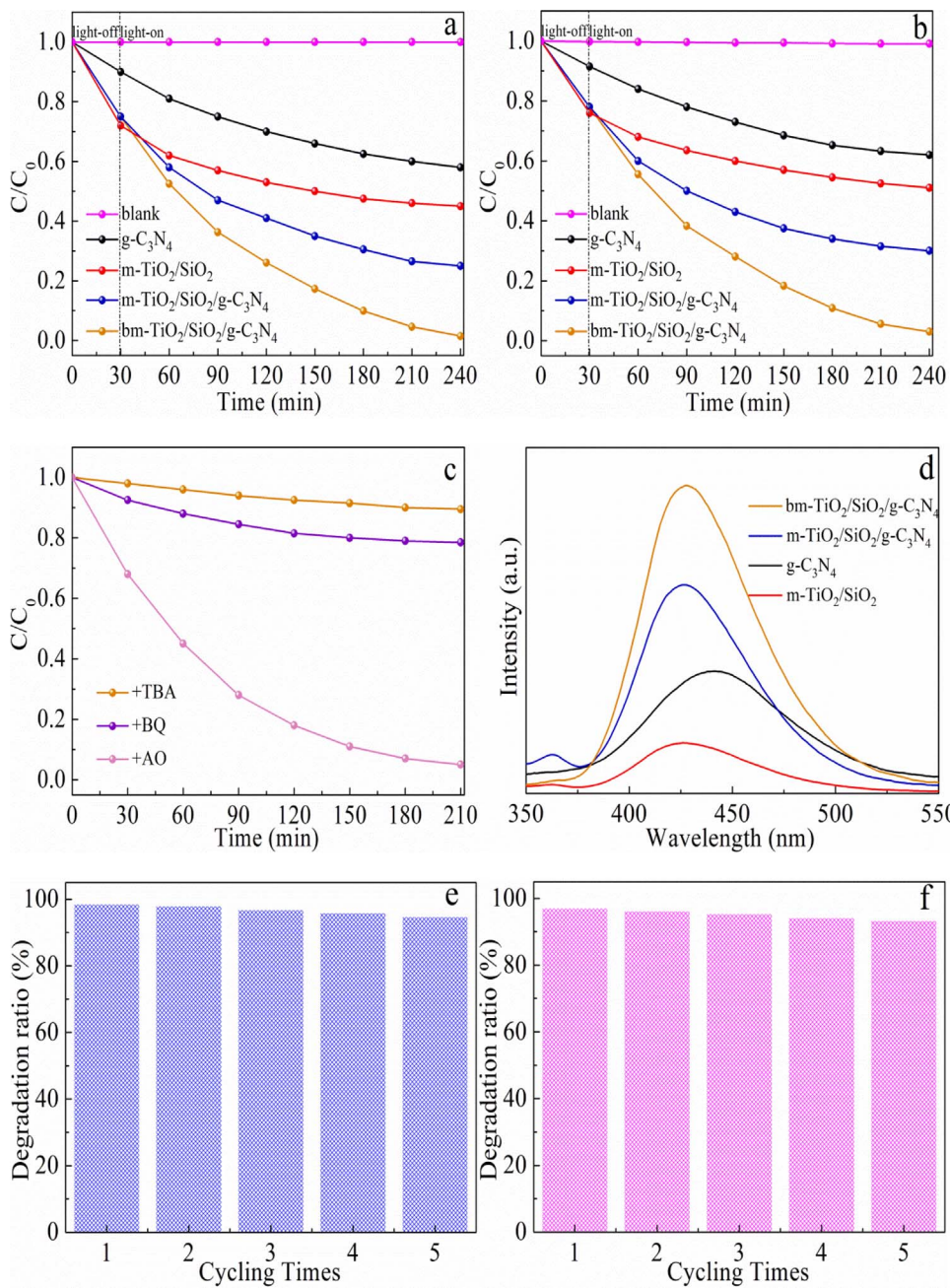


Fig. 6. The photodegradation of phenol (a) and reduction of Cr⁶⁺ (b) under visible-light irradiation, the fluorescence intensity after visible light irradiation for 1 h (d) of g-C₃N₄, m-TiO₂/SiO₂, m-TiO₂/SiO₂/g-C₃N₄, and bm-TiO₂/SiO₂/g-C₃N₄, respectively. The photocatalytic degradation of phenol under the condition of adding different trapping agents (c), the cycles of phenol photocatalytic degradation (e), and reduction of Cr⁶⁺ (f) of bm-TiO₂/SiO₂/g-C₃N₄.

irradiation. A blank sample without any catalyst is also tested to demonstrate the photocatalytic activity of the catalyst. We can obviously notice that the self-degradation process is almost negligible after 240 min, implying that the phenol and Cr⁶⁺ are considerably stable and the degradation and reduction through itself is negligible. Fig. 6a shows the degradation of phenol pollutants by four photocatalysts. Before the visible light irradiation, an adsorption-desorption equilibrium measurement is established to evaluate excellent adsorption properties of mesoporous materials. In the process of dark adsorption, the incipient phenol can be eliminated 10, 28, 25, and 25% with the g-C₃N₄, m-TiO₂/SiO₂, m-TiO₂/SiO₂/g-C₃N₄, and bm-TiO₂/SiO₂/g-C₃N₄, respectively. The m-TiO₂/SiO₂, m-TiO₂/SiO₂/g-C₃N₄, and bm-TiO₂/SiO₂/g-C₃N₄ photocatalysts have outstanding adsorption performance, because they have both mesoporous structure with large surface area owing to the introduction of SiO₂, which can enhance the adsorption of pollutants. After visible light irradiation for 120 min, the m-TiO₂/SiO₂/g-C₃N₄, and bm-TiO₂/SiO₂/g-C₃N₄ photocatalysts show the inconceivable

photocatalytic degradation efficiency than that of g-C₃N₄ and m-TiO₂/SiO₂ samples. In especial, the bm-TiO₂/SiO₂/g-C₃N₄ demonstrates the inapproachable photocatalytic degradation ability, which can reach 98.5% for phenol. Similarly, the bm-TiO₂/SiO₂/g-C₃N₄ sample is still the most prominent for the reduction of Cr⁶⁺ (in Fig. 6b), which can degrade to 20% in the dark absorption and reduction to 97% in the photodegradation process. In order to further prove the activity of photocatalyst for the mineralization of phenol pollutants, the TOC is carried out. It is clearly shown in Fig. S1 that the initial TOC removal efficiency is up to 97% from the phenol aqueous solution by bm-TiO₂/SiO₂/g-C₃N₄, indicating that bm-TiO₂/SiO₂/g-C₃N₄ has the highest activity toward phenol pollutants mineralization (conversion to H₂O and CO₂). The transcendental photocatalytic efficiency of the bm-TiO₂/SiO₂/g-C₃N₄ is attributed to the self-doping of Ti³⁺, and the synergistic effects of bm-TiO₂/SiO₂ and g-C₃N₄, which can accelerate the transfer efficiency of photogenerated electrons and reduce the recombination rate of electrons and holes. The pollutants are degraded by different

kinds of free radicals that are excited by visible light. The electron spin resonance (ESR) with 5,5-dimethyl-1-pyrroline *N*-oxide (DMPO) is employed to evaluate the species of active radicals involved in the reactions. Fig. S2. shows the obvious ESR signals of DMPO – ·OH and DMPO – ·O₂[–] of bm-TiO₂/SiO₂/g-C₃N₄ samples under visible light illumination, indicating that the main free radicals involved in the degradation reaction are ·OH and ·O₂[–]. In order to explore the effect of free radicals for the degradation of pollutants, ammonium oxalate (AO), benzoquinone (BQ), and *tert*-butyl alcohol (TBA) are used capture agent to capture h⁺, ·O₂[–], and ·OH respectively. As explained in Fig. 6c, the addition of TBA can weaken photocatalytic efficiency to a great extent compared to the addition of AO and BQ, implying that ·OH can take a decisive role on photocatalytic decomposition of contaminant. ·O₂[–] has a secondary role and the effect of h⁺ is relatively low. In order to identify the ability of these sample to produce ·OH, fluorescence (FL) is performed. Terephthalic acid (TA) is elected as a fluorescenceprobe owing to the fact that it can react with ·OH in fundamental solution to produce 2-hydroxy terephthalic acid (TAOH), in which the fluorescence signal at about 425 nm. As shown in Fig. 6d, the fluorescence intensity of bm-TiO₂/SiO₂/g-C₃N₄ photocatalyst is the highest in four samples at 425 nm, it is a powerful explanation that the bm-TiO₂/SiO₂/g-C₃N₄ photocatalyst has the most highlighted capacity to generate ·OH under visible light illumination, consisting with the preeminent photocatalytic degradation results of phenol and reduction of Cr⁶⁺. Furthermore, in order to verify the degradation stability of the bm-TiO₂/SiO₂/g-C₃N₄ photocatalyst, the phenol and Cr⁶⁺ solution are cyclically degraded by the bm-TiO₂/SiO₂/g-C₃N₄, as shown in Fig. 6e and f, respectively. After five cycles, the photocatalytic activity of bm-TiO₂/SiO₂/g-C₃N₄ sample is almost no decrease, indicating that its photocatalytic stability is wonderful.

The brilliant photocatalytic activity of the bm-TiO₂/SiO₂/g-C₃N₄ material is also tested through the photocatalytic decomposition of water for hydrogen evolution under the visible light irradiation. As indicated in Fig. 7a, the H₂ evolution rates of g-C₃N₄ and m-TiO₂/SiO₂ only show 103.6 and 65.8 μmol h^{–1} g^{–1}, respectively. However, m-TiO₂/SiO₂/g-C₃N₄ with hydrogen evolution rates of 395.5 μmol h^{–1} g^{–1} is about 6 folds higher than that of pristine m-TiO₂/SiO₂ without g-C₃N₄, which is mainly due to the fact that the addition of g-C₃N₄ can form heterojunction with m-TiO₂/SiO₂, accelerate the dispersion and transfer of photogenerated charge carriers, and improve the survival efficiency of various free radicals. Moreover, it is very satisfying that the bm-TiO₂/SiO₂/g-C₃N₄ with hydrogen evolution rates of 572.6 μmol h^{–1} g^{–1} has the highest photocatalytic hydrogen production performance among these catalysts. Since Pt is an excellent hydrogen-producing cocatalyst, it is necessary to further demonstrate the ability of the synthesized visible-light-driven photocatalysts for hydrogen production. The contrast experiment is measured for the samples without the adding of Pt, as shown in Fig. S3. The H₂ evolution rates of g-C₃N₄, m-TiO₂/SiO₂, m-TiO₂/SiO₂/g-C₃N₄, and bm-TiO₂/SiO₂/g-C₃N₄ show 23.6, 5.35, 36.2, and 61.8 μmol h^{–1} g^{–1}, respectively, it is convincing that all samples have the ability to produce hydrogen without the participation of Pt and the performance of hydrogen production of bm-TiO₂/SiO₂/g-C₃N₄ is still the best one. The appearance of this extraordinary performance is due to three reasons, as follows: (1) The addition of SiO₂ can effectively protect the mesoporous structure and avoid the collapse of the pore channel. The presence of the mesoporous framework can increase the specific surface area of the catalyst and the surface active site. Further, the open pores are favorable for the refraction of visible light and transmission of electrons, and ultimately improve the photocatalytic efficiency. (2) The formation of heterojunction between m-TiO₂/SiO₂ and g-C₃N₄ can accelerate electron transfer and prevent the recombination of electron and hole. (3) The Ti³⁺ self-doping can form a new doping level between the valence band and the conduction band of mesoporous TiO₂, and then narrow the band gap of the material, and finally enhance the absorption and the effective utilization of visible light. Fig. 7b shows the cycling test for

H₂ production to assess the photocatalytic stability of the bm-TiO₂/SiO₂/g-C₃N₄. We can clearly note that the hydrogen production efficiency of the bm-TiO₂/SiO₂/g-C₃N₄ has almost no change after 5 cycles, indicating that the high stability of the bm-TiO₂/SiO₂/g-C₃N₄ sheets heterojunctions.

In order to analysis the separation ability of these samples to produce charge carriers, transient photocurrent response is performed. As shown in Fig. 7c, the transient photocurrent response of bm-TiO₂/SiO₂/g-C₃N₄ is the highest among other photocatalysts and there is no doubt that bm-TiO₂/SiO₂/g-C₃N₄ has the most remarkable photoelectric ability, which is due to the synergistic effect of the emergence of mesoporous structures, the formation of heterojunctions between m-TiO₂/SiO₂ and g-C₃N₄, and the introduction of Ti³⁺ self-doping. What is more, Fig. 7d shows electrochemical impedance spectroscopy (EIS) of g-C₃N₄, m-TiO₂/SiO₂, m-TiO₂/SiO₂/g-C₃N₄, and bm-TiO₂/SiO₂/g-C₃N₄ composite materials that can precise and effective measure electrical conductivity of charge carriers. The electrochemical impedance test of the bm-TiO₂/SiO₂/g-C₃N₄ shows smaller semicircle than that of others, implying that bm-TiO₂/SiO₂/g-C₃N₄ owns a more efficient and faster charge separation. This implies that the mesoporous materials with open channels can provide a convenient way for rapid transfer of electrons and reduce transmission resistance. Simultaneously, g-C₃N₄ and self-doped Ti³⁺ also account for the reinforce the conductivity of electrons, leading to smaller impedance and higher electroconductibility.

To further explore the presence of Ti³⁺, the low temperature electron paramagnetic resonance (EPR) is measured. As indicated in Fig. 7e, it is obvious that two peaks appear at g = 1.943 and 2.002, which can be ascribe to the appearance of Ti³⁺ and oxygen vacancies, respectively. It is known that the Ti³⁺ on the surface of the photocatalyst are easily oxidized when they are exposed in the air and water, so the surface Ti³⁺ are unstable. However, Fig. 7e shows two poignant EPR signal, implying that most of the Ti³⁺ exist in the bulk of the bm-TiO₂/SiO₂/g-C₃N₄ sample. It can strengthen the stability of black mesoporous TiO₂/SiO₂/g-C₃N₄ in the environment.

The scanning kelvin probe (SKP) is sensitive to discern subtle molecular interactions by the vibrating electromagnetic and acoustic fields, which shows a relatively flat potential change according to the work function. As shown in Fig. 7f, the work functions of A, B, and C are 5.67, 5.57, and 5.20 eV, respectively. Since the work function of bm-TiO₂/SiO₂/g-C₃N₄ (~ 5.20 eV) is distinct lowest, the approximate Fermi level of bm-TiO₂/SiO₂/g-C₃N₄ is higher than that of m-TiO₂/SiO₂ and g-C₃N₄, which enhances the built-in electric field, surface band bending, and the effectiveness of escape of photogenerated electrons. Therefore, the effective separation of photogenerated charge and hole improves the photocatalytic performance of bm-TiO₂/SiO₂/g-C₃N₄ photocatalyst.

On the basis of the above discussion, the photocatalytic mechanism of bm-TiO₂/SiO₂/g-C₃N₄ heterojunctions photocatalyst is presented as illustrated in Fig. 8, the introduction of self-doped Ti³⁺ can form a new impurity level below the conduction band of bm-TiO₂/SiO₂, which can successfully narrow the band gap of the catalyst and thereby enhance the photoresponse, extending from UV light to visible light region. Simultaneously, the formation of heterojunctions between m-TiO₂/SiO₂ and g-C₃N₄ is also an important factor that can not be ignored to improve photocatalytic efficiency because the heterojunctions become a crucial bridge for the transfer of electrons and the separation of photogenerated electron-hole pairs. When the catalyst is excited, a large amount of photogenerated electrons produced on the valence band (VB) of bm-TiO₂/SiO₂ are immediately transferred to the conduction band (CB) of bm-TiO₂/SiO₂, leaving behind the holes in the VB of bm-TiO₂/SiO₂. The holes in the VB of the bm-TiO₂/SiO₂ can be moved to the VB of g-C₃N₄, and the electrons on the VB of the g-C₃N₄ can be rapidly excited to the CB of the g-C₃N₄, and eventually transferred to the CB of bm-TiO₂/SiO₂. The photo-generated electrons on the CB of bm-TiO₂/SiO₂ samples can react with O₂ and H₂O to generate ·O₂[–] and H₂, while OH[–]/H₂O are captured by holes in the VB of g-C₃N₄ to produce ·

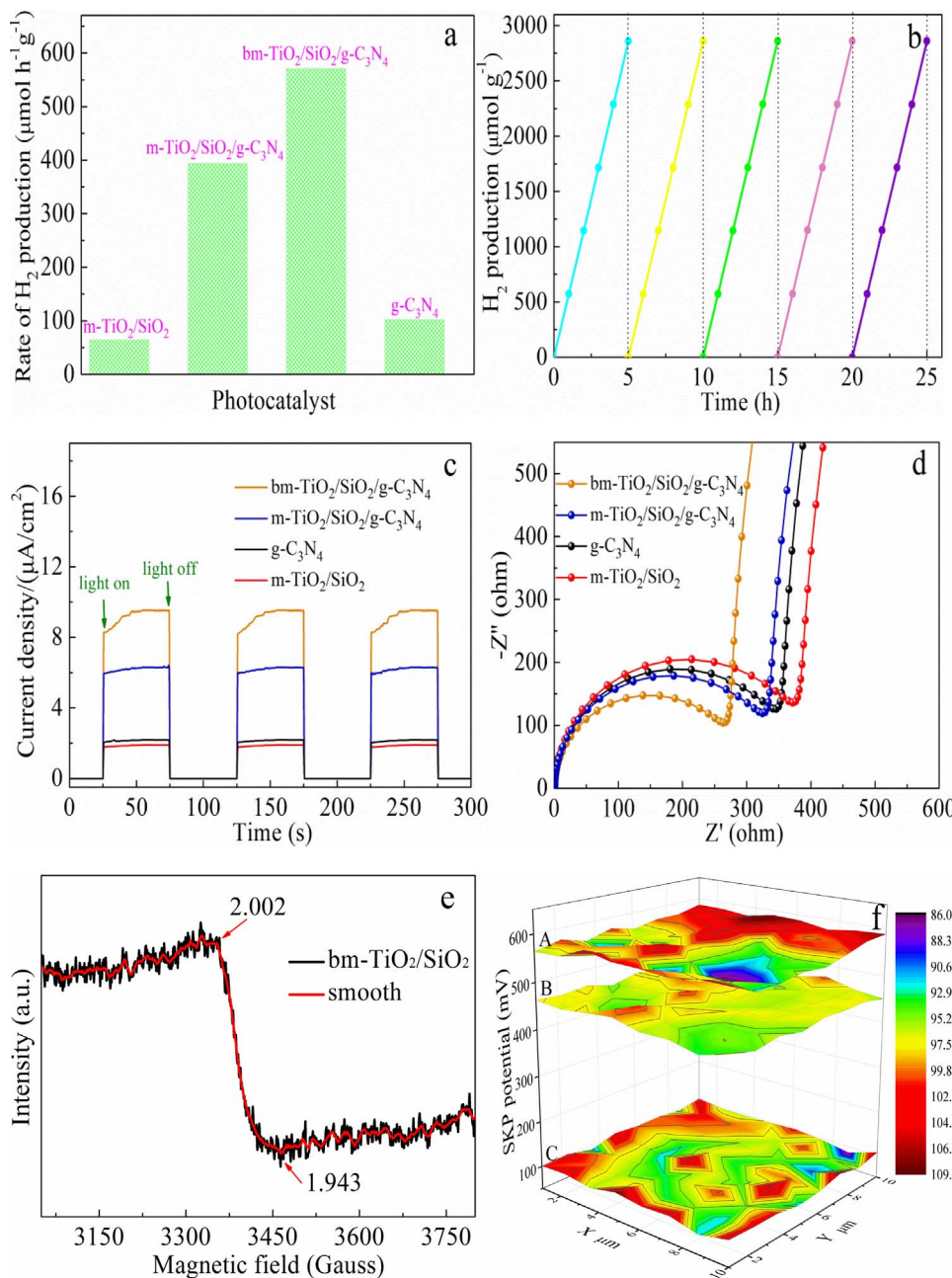


Fig. 7. The photocatalytic hydrogen evolution under visible-light irradiation (a), the transient photocurrent responses (c), and the nyquist plots (d) of g-C₃N₄, m-TiO₂/SiO₂, m-TiO₂/SiO₂/g-C₃N₄, and bm-TiO₂/SiO₂/g-C₃N₄, respectively. The cycle runs for the photocatalytic H₂ production (b) and the low temperature EPR (e) of the bm-TiO₂/SiO₂/g-C₃N₄ sample. The scanning kelvin probe maps (f) of m-TiO₂/SiO₂ (A), g-C₃N₄ (B), bm-TiO₂/SiO₂/g-C₃N₄ (C), respectively.

OH. Eventually, the pollutants are degraded by free radicals of $\cdot\text{O}_2^-$ and $\cdot\text{OH}$. This rapid circulation system of electronic and hole not only accelerates the transfer of electrons but also reduces the recombination rate of electrons and holes. In addition, the mesoporous structure with SiO₂ protection contributes to the positive effect for improving the photocatalytic performance due to its large specific surface area, which can increase the surface active site and favor the adsorption of contaminants. Therefore, the existence of mesoporous networks, the heterojunctions between m-TiO₂/SiO₂ and g-C₃N₄, and the introducing of self-doped Ti³⁺ can synergistically strengthen the photocatalytic activity.

4. Conclusions

In summary, Ti³⁺ self-doped mesoporous black TiO₂/SiO₂/g-C₃N₄ sheets heterojunctions were successfully synthesized via a sol-gel reaction, followed by calcination and surface hydrogenation strategy. The consequence showed that the mesoporous TiO₂/SiO₂ composite

photocatalyst with unique mesoporous structure of high surface area, uniform pore size, open pore channel, and large pore volume was successfully doped with Ti³⁺, meanwhile coupled with g-C₃N₄ sheets to form the heterojunctions between bm-TiO₂/SiO₂ and g-C₃N₄. Significantly, the as-prepared bm-TiO₂/SiO₂/g-C₃N₄ composite materials showed unimaginable improvements for the photocatalytic degradation performance of phenol and reduction of Cr⁶⁺ under visible-light irradiation. Meanwhile, the visible-light-driven photocatalytic H₂ production rate of bm-TiO₂/SiO₂/g-C₃N₄ were about 8 and 5 folds higher than that of m-TiO₂/SiO₂ and g-C₃N₄, respectively. The appearance of the splendid photocatalytic activity was attributed to the synergistic effect of the self-doping of Ti³⁺, the heterojunctions between m-TiO₂/SiO₂ and g-C₃N₄, and the existence of mesoporous structures with the SiO₂ protection, which can narrow the bandgap, promote the separation rate of photogenerated electrons and holes, increase the specific surface area and the surface activity sites, and ultimately improve the photocatalytic efficiency. Based on this research, we can believe that the unique Ti³⁺ self-doped mesoporous

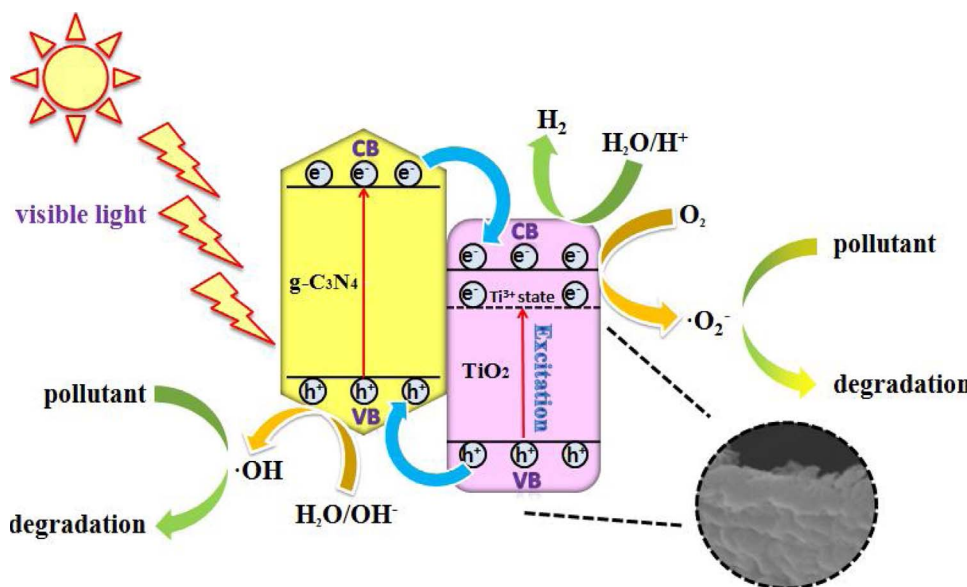


Fig. 8. The schematic illustration of photocatalytic mechanism for $\text{bm-TiO}_2/\text{SiO}_2/\text{g-C}_3\text{N}_4$ under visible light irradiation.

black $\text{TiO}_2/\text{SiO}_2/\text{g-C}_3\text{N}_4$ sheets heterojunctions will be a promising photocatalyst material, which will be well put into practical applications in future.

Acknowledgments

We gratefully acknowledge the support of this research by the National Natural Science Foundation of China (51672073 and 21376065), the Heilongjiang Postdoctoral Startup Fund (LBH-Q14135), the Postdoctoral Science Foundation of China (2017M611399), and the University Nursing Program for Young Scholars with Creative Talents in Heilongjiang Province (UNPYSCT-2015014, UNPYSCT-2016018).

Appendix A. Supplementary data

Supplementary data associated with this article can be found, in the online version, at <https://doi.org/10.1016/j.apcatb.2017.12.069>.

References

- W. Li, Q. Yue, Y.H. Deng, D.Y. Zhao, *Adv. Mater.* 25 (2013) 5129–5152.
- W. Li, M.B. Liu, S.S. Feng, X.M. Li, J.X. Wang, D.K. Shen, Y.H. Li, Z.K. Sun, A.A. Elzatahry, H.J. Lu, D.Y. Zhao, *Mater. Horiz.* 1 (2014) 439–445.
- Y.D. Liu, A.W. Tang, Q. Zhang, Y.D. Yin, *J. Am. Chem. Soc.* 137 (2015) 11327–11339.
- W. Li, J.P. Yang, Z.X. Wu, J.X. Wang, B. Li, S.S. Feng, Y.H. Deng, F. Zhang, D.Y. Zhao, *J. Am. Chem. Soc.* 134 (2012) 11864–11867.
- W. Zhou, T. Li, J.Q. Wang, Y. Qu, K. Pan, Y. Xie, G.H. Tian, L. Wang, Z.Y. Ren, B.J. Jiang, H.G. Fu, *Nano Res.* 7 (5) (2014) 731–742.
- Y. Cao, Z.P. Xing, Y.C. Shen, Z.Z. Li, X.Y. Wu, X. Yan, J.L. Zou, S.L. Yang, W. Zhou, *Chem. Eng. J.* 325 (2017) 199–207.
- H. Jeon, C.S. Lee, R. Patel, J.H. Kim, *ACS Appl. Mater. Interfaces* 7 (2015) 7767–7775.
- W.Y. Dong, Y.J. Sun, C.W. Lee, W.M. Hua, X.C. Lu, Y.F. Shi, S.C. Zhang, J.M. Chen, D.Y. Zhao, *J. Am. Chem. Soc.* 129 (2007) 13894–13904.
- M.Q. Hu, Y. Cao, Z.Z. Li, S.L. Yang, Z.P. Xing, *Appl. Surf. Sci.* 426 (2017) 734–744.
- Y.Q. Li, B.P. Bastakoti, M. Imura, S.M. Hwang, Z.Q. Sun, *J. Chem. Eur.* 20 (2014) 6027–6032.
- Y.B. Wang, Z.P. Xing, Z.Z. Li, X.Y. Wu, G.F. Wang, W. Zhou, *J. Colloid Interface Sci.* 485 (2017) 32–38.
- H.Y. Min, X.Q. Ran, J.W. Fan, Y. Sun, J.P. Yang, W. Teng, W.X. Zhang, G.M. Lia, D.Y. Zhao, *J. Mater. Chem. A* 3 (2015) 7399–7405.
- W. Zhou, W. Li, J.Q. Wang, Y. Qu, Y. Yang, Y. Xie, K.F. Zhang, L. Wang, H.G. Fu, D.Y. Zhao, *J. Am. Chem. Soc.* 136 (2014) 9280–9283.
- J. Tian, P. Hao, N. Wei, H.Z. Cui, H. Liu, *ACS Catal.* 5 (2015) 4530–4536.
- H. Kim, D.M. Satoca, W. Kim, W.Y. Choi, *Energy Environ. Sci.* 8 (2015) 247–257.
- W. Li, F. Wang, S.S. Feng, J.X. Wang, Z.K. Sun, B. Li, Y.H. Li, J.P. Yang, A.A. Elzatahry, Y.Y. Xia, D.Y. Zhao, *J. Am. Chem. Soc.* 135 (2013) 18300–18303.
- K.H. Ye, Z.L. Wang, J.W. Gu, S. Xiao, Y.F. Yuan, Y. Zhu, Y.M. Zhang, W.J. Mai, S.H. Yang, *Energy Environ. Sci.* 10 (2017) 772–779.
- X.F. Liu, Z.P. Xing, Y. Zhang, Z.Z. Li, X.Y. Wu, S.Y. Tan, X.J. Yu, Q. Zhu, W. Zhou, *Appl. Catal. B* 201 (2017) 119–127.
- Z.F. Jiang, C.Z. Zhu, W.M. Wan, K. Qian, J.M. Xie, *J. Mater. Chem. A* 4 (2016) 1806–1818.
- J.Y. Su, P. Geng, X.Y. Li, Q.D. Zhao, X. Quan, G.H. Chen, *Nanoscale* 7 (2015) 16282–16289.
- R.A. Rather, S. Singh, B. Pal, *Appl. Catal. B* 213 (2017) 9–17.
- R.R. Hao, G.H. Wang, H. Tang, L.L. Sun, C. Xu, D.Y. Han, *Appl. Catal. B* 187 (2016) 47–58.
- X.B. Chen, L. Liu, F.Q. Huang, *Chem. Soc. Rev.* 44 (2015) 1861–1885.
- A. Naldoni, M. Aliotta, S. Santangelo, M. Marelli, F. Fabbri, *J. Am. Chem. Soc.* 134 (2012) 7600–7603.
- X.B. Chen, L. Liu, *Science* 311 (2011) 746–750.
- Y. Zhang, Z.P. Xing, X.F. Liu, Z.Z. Li, X.Y. Wu, J.J. Jiang, M. Li, Q. Zhu, W. Zhou, *ACS Appl. Mater. Interfaces* 8 (2016) 26851–26859.
- Y.F. Xu, C. Zhang, L.X. Zhang, X.H. Zhang, H.L. Yao, J.L. Shi, *Energy Environ. Sci.* 9 (2016) 2410–2417.
- T.Q. Lin, C.Y. Yang, Z. Wang, H. Yin, X.J. Lu, F.Q. Huang, J.H. Lin, X.M. Xie, M.H. Jiang, *Energy Environ. Sci.* 7 (2014) 967–972.
- L.L. Zhang, Z.P. Xing, H. Zhang, Z.Z. Li, X.Y. Wu, D.Z. Zhang, Y. Zhang, W. Zhou, *Appl. Catal. B* 180 (2016) 521–529.
- Z.P. Xing, W. Zhou, F. Du, L.L. Zhang, Z.Z. Li, H. Zhang, W. Li, *ACS Appl. Mater. Interfaces* 6 (2014) 16653–16660.
- Y. Yang, M.R. Hoffmann, *Environ. Sci. Technol.* 50 (2016) 11888–11894.
- K. Panwar, M. Jassal, A.K. Agrawal, *RSC Adv.* 6 (2016) 92754–92764.
- X.B. Wei, C.L. Shao, X.H. Li, N. Lu, K.X. Wang, Z.Y. Zhang, Y.C. Liu, *Nanoscale* 8 (2016) 11034–11043.
- S.A. Ruettens, J.K. Thomas, *Photochem. Photobiol. Sci.* 2 (2003) 1018–1022.
- W.Y. Hu, W. Zhou, K.F. Zhang, X.C. Zhang, L. Wang, B.J. Jiang, G.H. Tian, D.Y. Zhao, H.G. Fu, *J. Mater. Chem. A* 4 (2016) 7495–7502.
- A.S. Nair, P.N. Zhu, V.J. Babu, S.Y. Yang, S.J. Peng, S. Ramakrishna, *RSC Adv.* 2 (2012) 992–998.
- J.J. Zhang, Z. Wei, T. Huang, Z.L. Liu, A.S. Yu, *J. Mater. Chem. A* 1 (2013) 7360–7369.
- L.Y. Shen, Z.P. Xing, J.L. Zou, Z.Z. Li, X.Y. Wu, Y.C. Zhang, Q. Zhu, S.L. Yang, W. Zhou, *Sci. Rep.* 7 (2017) 41978–41984.
- K. Li, S.M. Gao, Q.Y. Wang, H. Xu, Z.Y. Wang, B.B. Huang, Y. Dai, J. Lu, *ACS Appl. Mater. Interfaces* 7 (2015) 9023–9030.
- W. Li, F. Wang, Y.P. Liu, J.X. Wang, J.P. Yang, L.J. Zhang, A.A. Elzatahry, D. Al-Dahyan, Y.Y. Xia, D.Y. Zhao, *Nano Lett.* 15 (2015) 2186–2193.
- X.M. Zhou, N. Liu, P. Schmuki, *ACS Catal.* 7 (2017) 3210–3235.
- F. Zuo, L. Wang, T. Wu, Z.Y. Zhang, D. Borchardt, P.Y. Feng, *J. Am. Chem. Soc.* 132 (2010) 11856–11857.